Coexistence of superconductivity and magnetism in $Ca_{1-x}Na_xFe_2As_2$: Universal suppression of the magnetic order parameter in 122 iron pnictides

Philipp Materne,[1,*] Sirko Kamusella,[1] Rajib Sarkar,[1] Til Goltz,[1] Johannes Spehling,[1] Hemke Maeter,[1] Luminita Harnagea,[2] Sabine Wurmehl,[1,2] Bernd Büchner,[1,2] Hubertus Luetkens,[3] Carsten Timm,[4] and Hans-Henning Klauss[1,†]

[1]*Institute of Solid State Physics, TU Dresden, D-01069 Dresden, Germany*

[2]*Leibniz Institute for Solid State and Materials Research (IFW) Dresden, D-01069, Germany*

[3]*Laboratory for Muon Spin Spectroscopy, Paul Scherrer Institute, CH-5232 Villigen, Switzerland*

[4]*Institute of Theoretical Physics, TU Dresden, D-01069 Dresden, Germany*

(Received 5 May 2015; published 15 October 2015)

We present a detailed investigation of the magnetic and superconducting properties of $Ca_{1-x}Na_xFe_2As_2$ single crystals with $x = 0.00$, 0.35, 0.50, and 0.67 by means of the local probe techniques Mössbauer spectroscopy and muon spin relaxation experiments. With increasing Na-substitution level, the magnetic order parameter is suppressed. For $x = 0.50$ we find a microscopic coexistence of magnetic and superconducting phases accompanied by a reduction of the magnetic order parameter below the superconducting transition temperature T_c. A systematic comparison with other 122 pnictides reveals a square-root correlation between the reduction of the magnetic order parameter and the ratio of the transition temperatures T_c/T_N, which can be understood in the framework of a Landau theory. In the optimally doped sample with $T_c \approx 34$ K, diluted magnetism is found and the temperature dependence of the penetration depth and superfluid density are obtained, proving the presence of two superconducting s-wave gaps.

DOI: 10.1103/PhysRevB.92.134511 PACS number(s): 74.70.Xa, 76.75.+i, 76.80.+y, 74.62.Dh

I. INTRODUCTION

Since the discovery of superconductivity in iron pnictides [1], their electronic phase diagrams, characterized by a close proximity of magnetic and superconducting phases, have been explored in great detail. Of particular interest are the regions of the phase diagrams showing a crossover from magnetic order to superconductivity. Magnetic spin fluctuations, in particular if enhanced in the vicinity of a magnetic quantum critical point, can play an important role in the formation of Cooper pairs. In addition, the interplay of both magnetic order and superconductivity can lead to a phase with microscopic coexistence of both ground states [2–6]. As both states compete for the same electrons at the Fermi surface, the magnetic order parameter may be reduced below T_c [4–6]. In this work, we studied the system $Ca_{1-x}Na_xFe_2As_2$. The parent compound $CaFe_2As_2$ shows spin density wave order below the Néel temperature $T_N = 165$ K [7]. The magnetic phase transition is accompanied by a structural phase transition from a tetragonal to an orthorhombic structure [8]. Increasing the Na amount in $Ca_{1-x}Na_xFe_2As_2$, the magnetostructural phase transition is suppressed until it vanishes at a critical Na concentration $x \approx 0.35$ [7]. Superconductivity is found for $x \geqslant 0.3$ with a maximum of $T_c \approx 34$ K at an optimal doping of $x \approx 0.66$. However, the interaction of superconductivity with the magnetic spin density wave in the region of $0.3 \leqslant x \leqslant 0.35$ has not been conclusively determined.

We studied the magnetostructural phase transition as well as both the superconducting and the magnetic order parameter and their interaction for different Na-substitution levels. We find a suppression of the magnetostructural phase transition upon Na substitution.

For $x = 0.35$ and 0.50, microscopic coexistence of magnetic order and superconductivity is observed. For the latter Na-substitution level, a reduction of the magnetic order parameter is observed below the superconducting transition temperature. A systematic comparison with other 122 pnictides reveals a square-root correlation between the reduction of the magnetic order parameter and the ratio of the transition temperatures T_c/T_N, which can be understood in the framework of a Landau theory.

For $x = 0.67$, two superconducting gaps with s-wave symmetry can be deduced from the temperature dependence of the superfluid density.

II. EXPERIMENT

We examined mosaics of $Ca_{1-x}Na_xFe_2As_2$ single crystals, which were grown by the self-flux technique as described by Johnsten *et al.* [9]. The samples were characterized by energy-dispersive x-ray spectroscopy (EDX), x-ray diffraction (XRD), susceptibility, magnetization, and specific-heat measurements. The stoichiometry of the examined samples is $x = 0.00$, 0.35, 0.50, and 0.67 as determined by EDX. A characterization of the magnetic properties was performed using SQUID magnetometry in large and small external magnetic fields. Mössbauer spectroscopy (MBS) experiments were performed in transmission geometry in a temperature range between 4.2 and 300 K using a CryoVac Konti IT cryostat. As the γ source, a ^{57}Co in rhodium matrix was used.

The single crystals were aligned with the crystallographic c axis along the γ direction. To analyze the data, the hyperfine Hamiltonian including electric quadrupole and magnetic hyperfine interactions was diagonalized. In the paramagnetic temperature regime, the spectra were described by a doublet pattern, whereas in the magnetically ordered state a sextet pattern was used. The magnetic order parameter is deduced

*philipp.materne@tu-dresden.de
†h.klauss@physik.tu-dresden.de

from the ^{57}Fe magnetic hyperfine field $B_{\rm hf}$. The isomer shift δ is given with respect to α-Fe.

Muon spin relaxation (μSR) experiments were performed at the πM3 and PiE1 beamlines of the Swiss Muon Source at the Paul Scherrer Institut, Switzerland, using the GPS and DOLLY spectrometers. The single crystals were aligned with the crystallographic c axis along the muon beam. Positively charged muons μ^+, which are nearly 100% spin polarized due to parity violation during the pion decay, are implanted in the sample and thermalize at interstitial lattice sites, where they radioactively decay with a lifetime of 2.2 μs into two neutrinos and one positron. As the muon decay involves the weak interaction, where parity conservation is violated, the positron is predominantly emitted along the direction of the muon spin at the moment of the decay. Measuring the time-resolved angular distribution of the emitted positrons allows to extract the time evolution of the muon spin polarization $P(t)$. The initial muon spin was rotated by approximately -45° with respect to the beam, which allows to measure the time evolution of the muon spin polarization $\perp c$ and $\parallel c$ by analyzing the asymmetry of the up-down and forward-backward detector pair, respectively. If not stated otherwise, all presented measurements refer to the up-down detector pair. The muon spin relaxation was measured for temperatures ranging from 1.6 up to 300 K in zero field (ZF) and transverse magnetic fields (TF) up to 130 mT. The μSR data were analyzed using the MUSRFIT software package [10].

In a magnetically ordered material, the muon spin exhibits a Larmor precession with a frequency ν_μ, which is related to the local magnetic field B at the muon site by $\nu_\mu = B\gamma_\mu/(2\pi)$ (muon gyromagnetic ratio $\gamma_\mu = 2\pi \times 135.5$ MHz/T). The muon spin precession can be described in single crystals using the function [11]

$$P(t) = \sum_{i=1}^{N} P(\nu_i)[A_i \cos(\nu_i t)e^{-\lambda_T^i t} + (1 - A_i)e^{-\lambda_L^i t}], \quad (1)$$

with N denoting the number of inequivalent muon sites contributing to the μSR signal, weighted by $P(\nu_i)$. In the case of 100% magnetic ordering, $\sum P(\nu_i) = 1$. A_i describes the oscillating part of the signal. In contrast to powder samples, where $A_i = \frac{2}{3}$ due to spatial averaging, for single crystals $A_i \in [0,1]$. λ_T, describing the damping of the oscillation, is a measure of the width of the static field distribution, also including dynamic contributions due to magnetic fluctuations. The damping of the nonoscillating part, described by λ_L, is caused by dynamic magnetic fluctuations only [12].

To study the superconducting properties of the sample with μSR, a magnetic field $\mu_0 H_{\rm ext}$ was applied parallel or perpendicular to the muon beam. In type-II superconductors, a vortex lattice is formed for $\mu_0 H_{c1} < \mu_0 H_{\rm ext} < \mu_0 H_{c2}$ resulting in a spatial magnetic field distribution [13]. This magnetic field distribution causes an additional damping of the muon spin oscillation, which can be modeled via additional Gaussian terms of the form [13]

$$P(t) = \sum_{i=1}^{N} [P_i \cos(\gamma_\mu B_i t + \varphi)e^{-\frac{1}{2}\sigma_i^2 t^2}]e^{-\frac{1}{2}\sigma_N^2 t^2}, \quad (2)$$

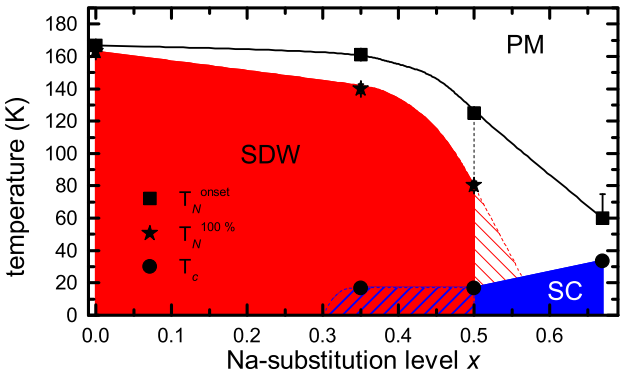

FIG. 1. (Color online) Phase diagram of $Ca_{1-x}Na_xFe_2As_2$ obtained by Mössbauer spectroscopy, muon spin relaxation, and magnetic susceptibility measurements. The evolution of $T_N^{100\%}$ for $x > 0.50$ is not known. The magnetic order is suppressed as a function of the Na-substitution level x. The temperature width of the magnetic phase transition $\Delta T = T_N^{\rm onset} - T_N^{100\%}$ increases as a function of x due to the enhanced degree of disorder due to the Na substitution. For $x = 0.35$, 0.50, and 0.67, nanoscopic coexistence of magnetic order and superconductivity is found below T_c. The blue-red shaded area denotes the temperature and Na-substitution level range, where 100% of the sample show magnetic order and parts ($x = 0.35$) or the whole sample volume ($x = 0.50$) are superconducting.

where σ_i describes the damping due to superconductivity, σ_N the damping due to nuclear magnetic dipole contributions, and φ denotes the angle between the initial muon spin direction and the positron detector. The second moment $\langle \Delta B^2 \rangle$ of the internal magnetic field distribution $n(B)$ is given by [13]

$$\langle \Delta B^2 \rangle = \sum_{i=1}^{N} \frac{A_i}{\sum_{i=1}^{N} A_i} \left[\left(\frac{\sigma_i}{\gamma_\mu} \right)^2 + (B_i - \langle B \rangle)^2 \right] \quad (3)$$

and related to the London penetration depths λ by the relation [14]

$$\langle \Delta B^2 \rangle = 0.00371 \Phi_0^2 \frac{1}{\lambda^4}, \quad (4)$$

where Φ_0 denotes the magnetic flux quantum. λ is related to the Cooper pair density by $n_s \propto 1/\lambda^2$.

Therefore, μSR allows to independently measure the magnetic and superconducting order parameters via the determination of the zero-field muon spin precession frequency ν_i and the London penetration depth, respectively. Moreover, μSR is able to distinguish between nonmagnetic and magnetic volume fractions in the sample.

III. RESULTS AND DISCUSSION

The electronic phase diagram of $Ca_{1-x}Na_xFe_2As_2$ obtained by Mössbauer spectroscopy, muon spin relaxation, and magnetic susceptibility measurements is shown in Fig. 1. Measurements of the magnetic susceptibility of $CaFe_2As_2$ are reported by Harnagea *et al.* [15]. Magnetic susceptibility measurements in an applied field of 1 T parallel to the *ab* plane are shown in Fig. 2. For $x = 0.00, 0.35, 0.50$, and 0.67, a nearly linear decrease of the magnetic susceptibility is observed in the paramagnetic region, which is found also for many other iron pnictides [16–18]. The kink at 167, 143, 119, and 150 K

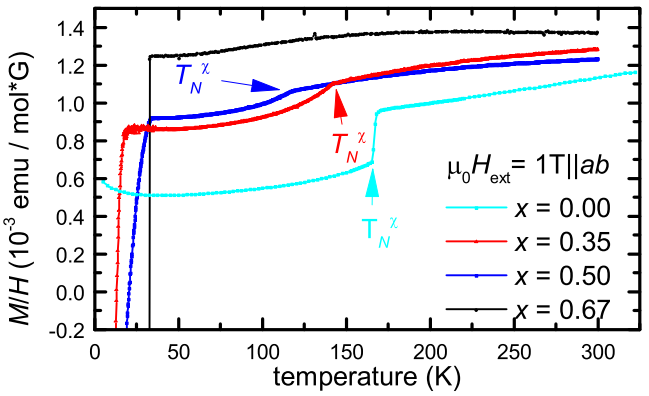

FIG. 2. (Color online) Temperature dependence of the static susceptibility $\chi = M/H$ of $Ca_{1-x}Na_xFe_2As_2$ for $x = 0.00$, 0.35, 0.50, and 0.67. The measurements were performed at an applied field of 1 T parallel to the *ab* plane. T_N^χ denotes the magnetic transition temperature. Data for $x = 0.00$ are taken from Ref. [15].

for $x = 0.00$, 0.35, 0.50, and 0.67, respectively, indicates the onset of the antiferromagnetic (AFM) ordering. Magnetic susceptibility measurements in an applied field of 2 mT parallel to the *ab* plane are shown in Fig. 3. For $x = 0.35$, below 17 K a broad superconducting transition occurs. As the diamagnetic shielding is not fully developed, only parts of the sample show superconductivity. For $x = 0.50$, a two-step superconducting transition occurs. Below 34 K, a slightly negative magnetic susceptibility is measured, which indicates a superconducting phase in a small volume of the sample. Below 17 K, a broad second transition occurs, where bulk superconductivity is formed resulting in the full superconducting response. For the further treatment of the $x = 0.50$ sample, 17 K will be considered as the superconducting transition temperature. This two-step behavior as well as the broad transition indicates an inhomogeneous sample. The sample with $x = 0.67$ shows bulk superconductivity below 34 K. The sharp transition indicates a homogeneous sample.

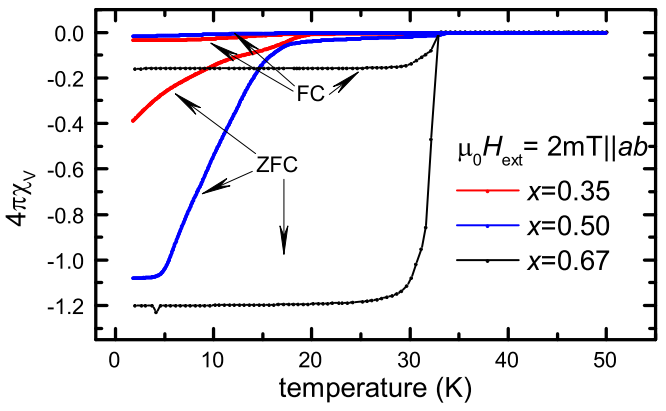

FIG. 3. (Color online) Temperature dependence of the magnetic susceptibility χ_v [zero field cooled (ZFC) and field cooled (FC)] of $Ca_{1-x}Na_xFe_2As_2$ for $x = 0.35$, 0.50, and 0.67. The measurements were performed at an applied field of 2 mT parallel to the *ab* plane.

TABLE I. Low-temperature saturation values of ν_A and B_{hf} of the undoped compounds $CaFe_2As_2$, $SrFe_2As_2$, and $BaFe_2As_2$. A systematic reduction of the magnetic moment and therefore of the muon spin precession frequency and the magnetic hyperfine field as a function of the ionic radius of the alkaline-earth metal [24] is observed.

	ν_A/MHz	B_{hf}/T
$CaFe_2As_2$	52	10.1 [20]
$SrFe_2As_2$	44 [21]	8.9 [22]
$BaFe_2As_2$	28.8 [19]	4.4 [23]

A. Magnetic order in $CaFe_2As_2$

The time evolution of the muon spin polarization in ZF is shown in Fig. 4. Analyzing the up-down detector pair, the muon spin polarization perpendicular to the crystallographic *c* axis is investigated. Therefore, static local magnetic fields *B* parallel to *c* can be detected. In the paramagnetic temperature regime, a weak Gauss-Kubo-Toyabe damping of the signal is observed caused by the dipole-dipole interaction of the muon magnetic moment with randomly oriented nuclear magnetic moments. The temperature dependence of the magnetic volume fraction (MVF) is shown in Fig. 5. To describe MVF as a function of T, two temperatures are defined: T_N^{onset} describes the highest temperature with a finite MVF and $T_N^{100\%}$ describes the highest temperature with MVF $= 100\% \mathrel{\hat{=}} 1$. The sharp transition between $T_N^{\text{onset}} = 167$ K and $T_N^{100\%} = 163$ K indicates a homogeneous sample.

1. Two muon stopping sites

Below 167 K, two magnetically inequivalent muon stopping sites *A* and *B* with a temperature-independent occupation ratio of $P_A{:}P_B = 80{:}20$ were observed as it was found in $BaFe_2As_2$ [19]. The signal fraction corresponding to muons stopping at site *A* show a well-defined sinusoidal oscillation below 167 K. This indicates static long-range commensurate magnetic order. The temperature dependence of ν_A is shown in Fig. 6 and the low-temperature saturation value is compared to $SrFe_2As_2$ and $BaFe_2As_2$ in Table I. The steplike behavior indicates a first-order transition, as it was seen in $SrFe_2As_2$ [21].

The signal fraction corresponding to muons stopping at site *B* show an exponential relaxation below 167 K and a well-defined sinusoidal oscillation below 60 K. This indicates a broad field distribution at temperatures between 60 and 167 K at the muon stopping site *B* suppressing a coherent oscillation of the muon spins, which is contrary to the observations in $BaFe_2As_2$, where the two oscillation frequencies were obtained at all temperatures below T_N [19], but consistent with LaOFeAs [25].

Below 60 K, the two precession frequencies have a temperature-independent ratio of $\nu_A/\nu_B \approx 1.9$. Therefore, the magnetic field at the muon stopping site *A* is higher than on site *B*. Site *A* is located next to the FeAs layer [26]. The smaller value of the magnetic field at site *B* indicates a muon stopping site more distant from the FeAs layer. As the precession frequency is proportional to the magnetic field at the muon site, this ratio is different from $BaFe_2As_2$ [27] and $SrFe_2As_2$ [21], showing ratios of 4.1 and 3.4, respectively. The ionic radii

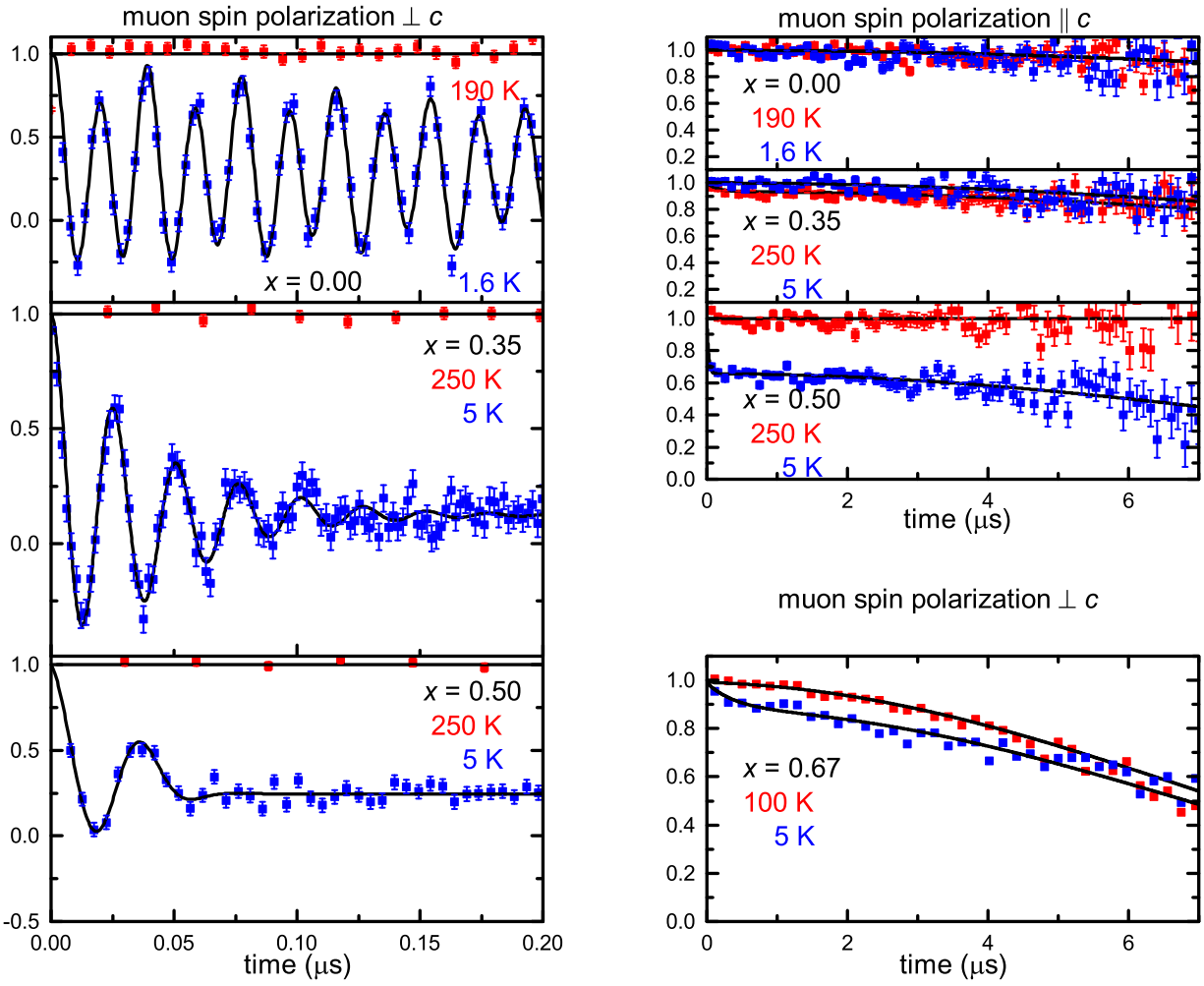

FIG. 4. (Color online) ZF-μSR time spectra of $Ca_{1-x}Na_xFe_2As_2$ for characteristic temperatures in the paramagnetic and magnetically ordered state for the muon spin components parallel and perpendicular to the crystallographic c axis. The well-defined muon spin precession of the muon spin component $\perp c$ for $x = 0.00$, 0.35, and 0.50 indicate long-range commensurate magnetic order. For $x = 0.67$, short-range magnetic order is found in small volume fractions at lowest measured temperatures. Solid lines are best fits according to Eq. (1).

of the alkaline-earth metals scale like Ca < Sr < Ba [24]. As a consequence, the crystallographic c axis is shortest for $CaFe_2As_2$ [7] and longest for $BaFe_2As_2$ [28]. By shrinking the crystallographic c axis, the distance between site B and the ordered iron magnetic moments in the FeAs layer is reduced. The muon spin interacts with the ordered electronic moments via dipole-dipole and transferred Fermi-contact interaction. Both interactions are sensitive to the distance between the muon spin and the iron ordered moments. This implies that the change of the frequency ratio in the undoped compounds has a structural origin.

2. *Orientation of the ordered magnetic moments*

Analyzing the forward-backward detector pair, the muon spin polarization parallel to the crystallographic c axis is investigated. A Gauss-Kubo-Toyabe depolarization is observed down to lowest temperatures. This, together with the oscillation measured in the up-down detector pair, proofs an orientation of the local magnetic field B along the crystallographic c axis. This is consistent with magnetic moments located in the ab plane.

Mössbauer measurements by Alzamora *et al.* [20] on $CaFe_2As_2$ show a first-order-like magnetostructural phase transition below 173 K. They report a saturated magnetic hyperfine field of ≈10.1 T at 4.2 K. The angle between the magnetic hyperfine field and the principal axis of the electric field gradient was reported as 94(4)°. Therefore, as the principal axis of the electric field gradient is parallel to the crystallographic c axis [20], the magnetic hyperfine field is located in the ab plane [20,29]. These Mössbauer results are consistent with our μSR results showing that the magnetic moments are located in the ab plane.

B. Magnetic order in $Ca_{0.65}Na_{0.35}Fe_2As_2$ and $Ca_{0.50}Na_{0.50}Fe_2As_2$

Mössbauer spectra for characteristic temperatures in the paramagnetic and magnetically ordered states are shown in Fig. 7. In the paramagnetic state, an asymmetric doublet structure, which is caused by the interaction of the nucleus with an electric field gradient (EFG), was observed for both stoichiometries. However, in the principal-axis system, the EFG is fully determined by its z component V_{zz} and the asymmetry parameter η (which turned out to be zero for all investigated

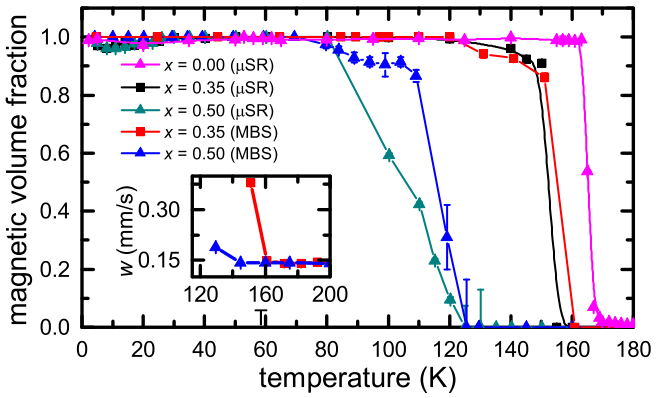

FIG. 5. (Color online) Magnetic volume fraction as a function of temperature (lines are guides to the eye only) of $Ca_{1-x}Na_xFe_2As_2$ obtained from ZF-μSR and Mössbauer spectroscopy for $x = 0.00$, 0.35, and 0.50. The inset shows the temperature dependence of the Mössbauer linewidth w. The abrupt increase of w indicates magnetic ordering.

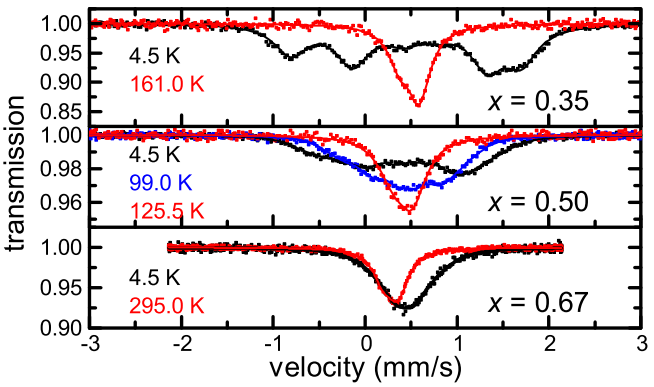

FIG. 7. (Color online) Mössbauer spectra of $Ca_{1-x}Na_xFe_2As_2$ for characteristic temperatures in the paramagnetic and magnetically ordered state. The sextet structure of the Mössbauer spectra for $x = 0.35$ and 0.50 indicate long-range commensurate magnetic order. For $x = 0.67$, a broadening below ≈150 K is observed, which cannot be described by a change in V_{zz} indicating small magnetic fields at the iron nucleus.

temperatures). At room temperature, for $x = 0.35$ and 0.50 a value of $V_{zz} = 11.2(5)$ V/Å^2 was obtained. This is similar to the reported room temperature value of $V_{zz} = 12(1)$ V/Å^2 for $x = 0.00$ [20]. With decreasing temperature, V_{zz} slightly increases to 13.0(5) V/Å^2 directly above the magnetic transition temperature as shown in Fig. 8. With the onset of magnetic order V_{zz} increases to 19(2) V/Å^2 and 18(3) V/Å^2 for $x = 0.35$ and 0.50, respectively, and remains constant within error bars down to lowest temperature. This increase was also observed in the undoped compound where V_{zz} increases to 22.6(7) V/Å^2 below the magnetostructural phase transition [20]. As the behavior of V_{zz} in the Na-substituted compounds with $x = 0.35$ and 0.50 is the same as in the undoped compound, we conclude that in these compounds a magnetostructural phase transition occurs. Furthermore, the principal axis of the EFG is parallel to the crystallographic c axis. The temperature dependence of the angle θ between the principal axis of the EFG and the magnetic hyperfine

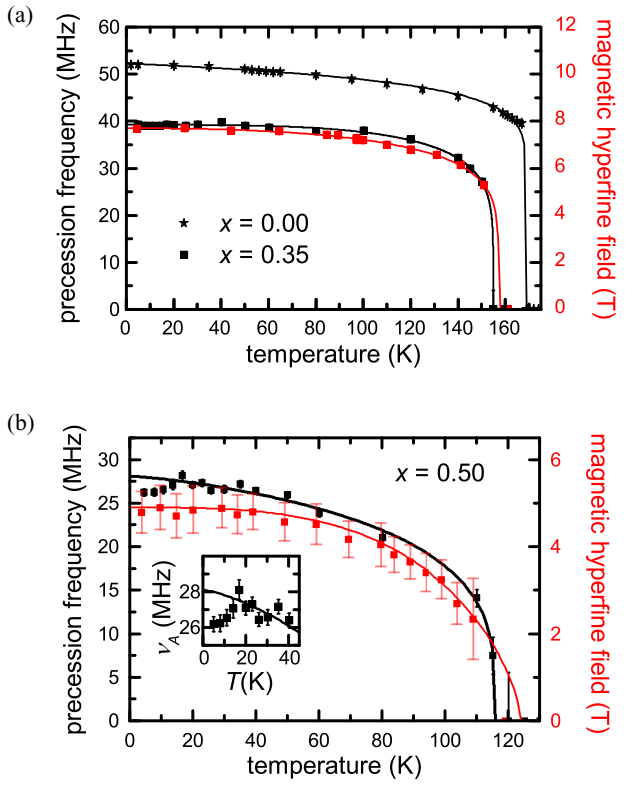

FIG. 6. (Color online) Temperature dependence of the magnetic order parameter for (a) $x = 0.00$ and 0.35 and (b) $x = 0.50$ including best order parameter fits according to Eq. (5). The magnetic hyperfine field for $x = 0.50$ is Gaussian distributed. The average value of the Gaussian distribution is shown with one standard deviation as error bar. The inset in (b) shows the low-temperature regime, where superconductivity occurs below $T_c = 17$ K.

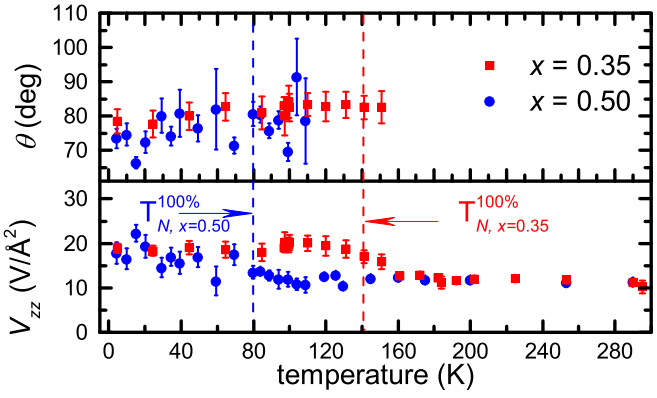

FIG. 8. (Color online) Temperature dependence of θ, the polar angle between the magnetic hyperfine field B_{hf} and the principal axis of the electric field gradient V_{zz}. The increase of V_{zz} indicates a change in the electromagnetic environment of the ^{57}Fe nucleus and corresponds to the magnetic phase transition. The vertical dashed lines denote the highest temperature, where the sample shows a MVF of 100%.

field, obtained from a fit to the data, is shown in Fig. 8. We have obtained $\theta = 80(5)^\circ$ and $71(5)^\circ$ for $x = 0.35$ and 0.50, respectively, in the fully ordered state. These values indicate a tilting of the magnetic moments out of the *ab* plane.

The time evolution of the muon spin polarization in ZF on $Ca_{1-x}Na_xFe_2As_2$ (with $x = 0.00$, 0.35, 0.50, and 0.67) is shown in Fig. 4. As for the parent compound described above, a weak Gauss-Kubo-Toyabe damping of the signal is observed caused by the dipole-dipole interaction of the muon magnetic moment with randomly oriented nuclear magnetic moments in the paramagnetic temperature regime. The onset of long-range commensurate magnetic ordering below $T_N^{\text{onset}} = 160(2)$ K and 125(3) K for $x = 0.35$ and 0.50, respectively, is indicated by the appearance of a well-defined muon spin precession with two frequencies ν_A and ν_B. The occupation probability is independent of the temperature and the Na-substitution level [$P(\nu_A)$:$P(\nu_B)$= 80:20]. We conclude that two magnetically inequivalent muon sites are present in a homogeneous magnetically ordered phase. The temperature dependence of the muon frequency ν_A for both samples is shown in Figs. 6(a) and 6(b). The onset temperature is consistent with the results of the macroscopic magnetization measurements by SQUID magnetometry. Analyzing the forward-backward detector pair, a signal fraction showing a fast exponential relaxation is observed in the magnetically ordered phase. This signal fraction increases as a function of the Na-substitution level from 0% to 5% and 35% for $x = 0.00$, 0.35, and 0.50, respectively. This is consistent with the tilting of the magnetic moments out of the *ab* plane as observed by Mössbauer spectroscopy.

1. Two muon stopping sites

The two frequencies have a temperature-independent ratio of $\nu_A/\nu_B \approx 4$ and 8 for $x = 0.35$ and 0.50, respectively, which are different compared to the undoped compound showing $\nu_A/\nu_B \approx 1.9$. This change is more drastic compared to other 122 compounds. It was discussed in Sec. III A that the change of the frequency ratio has a structural origin. The different substitution possibilities of the alkaline-earth metals Ca, Sr, and Ba by the alkaline metals Na and K lead to different structural effects. Their ionic radii scale like Ca < Na < Sr < Ba < K [24]. Substituting an alkaline-earth metal by an alkaline metal with a smaller ionic radius (Ba → Na, Sr → Na) results in a smaller change in the *c*-axis parameter compared to the substitution with an alkaline metal with a larger ionic radius (Ca → Na, Ba → K, Sr → K). $BaFe_2As_2$ shows a ratio of 4.1 [27], which increases to 4.47 for $Ba_{0.77}K_{0.23}Fe_2As_2$ [27] and 4.5 for $Ba_{0.7}Na_{0.3}Fe_2As_2$ [30]. $SrFe_2As_2$ shows a ratio of 3.4 [21], which changes to 3.6 for $Sr_{0.5}Na_{0.5}Fe_2As_2$ [31]. The change of the precession frequency ratio ν_A/ν_B in the case of substitution with a larger ion occurs at lower substitution levels than in the case of substitution with a smaller ion [7,21,28,30–33].

The change in the frequency ratio is connected to the crystallographic structure. By increasing the Na-substitution level in $Ca_{1-x}Na_xFe_2As_2$, the crystallographic *c* axis is elongated, resulting in an increased distance of the muon spin at the site *B* from the iron ordered moments in the FeAs plane. The muon spin interacts with the ordered electronic moments via dipole-dipole and transferred Fermi-contact interaction and both interactions are sensitive to the distance of muon spin and electronic moments, indicating a structural origin of the change of the frequency ratio. However, a change in the Fermi-contact interaction for both muon stopping sites cannot be ruled out and a small tilting of the magnetic moments out of the *ab* plane may also change the magnetic field at the muon site.

2. Magnetic volume fraction

The temperature dependence of the magnetic volume fraction was determined independently by ZF and TF μSR measurements as well as Mössbauer spectroscopy. TF μSR experiments were performed by applying a magnetic field of 5 mT perpendicular to the initial muon spin polarization. The temperature dependence of the MVF is shown in Fig. 5. The onset of the magnetic ordering is also indicated by the abrupt increase of the Mössbauer linewidth w due to the appearance of a magnetic hyperfine field. This increase is shown in the inset of Fig. 5 leading to $T_{\text{onset}} = 161(2)$ K and 125(3) K for $x = 0.35$ and 0.50, respectively. Therefore, the obtained characteristic temperatures of the magnetic phase transition are of equal value within error bars for both μSR and MBS and coincide with the magnetic phase transition temperature obtained by magnetic susceptibility measurements T_N^{χ}. The temperature width of the phase transition $\Delta T = T_N^{\text{onset}} - T_N^{100\%}$, increased from 4 to 21 and 45 K for $x = 0.00$, 0.35, and 0.50, respectively. We attribute this increased width of the magnetic phase transition to the increased degree of disorder due to the Na substitution. The MVF is constant below $T_N^{100\%} = 163(2)$, 140(3), and 80(3) K for $x = 0.00$, 0.35, and 0.50, respectively, proving bulk magnetic order.

3. Magnetic order parameter

In the magnetically ordered state, a well-resolved sextet was observed in the Mössbauer spectra for $x = 0.35$, as it is shown in Fig. 7 at $T = 4.5$ K. This proves a static commensurate magnetic ground state with a well-defined hyperfine field. For $x = 0.50$, the sextet is less clearly resolved and the spectra were modeled using a Gaussian distribution of magnetic hyperfine fields. This takes into account a higher degree of disorder than in the sample with $x = 0.35$. Consistently also the μSR transverse relaxation rate λ^T is largest for $x = 0.50$ as can be seen by a much faster suppression of the ZF oscillation in Fig. 4 compared to lower Na-substitution levels. The temperature dependence of the obtained magnetic hyperfine field of $x = 0.35$ is shown in Fig. 6(a). The temperature dependence of the mean value of the obtained Gaussian distributed magnetic hyperfine field B_{hf} for $x = 0.50$ is shown in Fig. 6(b).

Both ν_A and B_{hf} were analyzed using a fit to the temperature-dependent order parameter (M) of the form

$$M(T) = M(T = 0)\left[1 - \left(\frac{T}{T_N}\right)^{\alpha}\right]^{\beta} \tag{5}$$

for $x = 0.35$ and 0.50, respectively, above the superconducting transition temperatures (17 K in both cases).

TABLE II. Critical exponent β obtained by evaluating the temperature dependence of ν_A and $B_{\rm hf}$ using Eq. (5) with $\alpha = 1$.

	0.35		0.50	
x	ν_A	$B_{\rm hf}$	ν_A	$B_{\rm hf}$
β	0.13(3)	0.12(4)	0.24(4)	0.35(9)

For $x = 0.35$, a fit to Eq. (5) above T_c for both $\nu_A(T)$ and $B_{\rm hf}(T)$ represents the data in the whole temperature range, i.e., also below the superconducting transition. Therefore, no interaction between the magnetic and superconducting order parameter is detectable. For $x = 0.50$, the muon frequency is reduced by approximately 7% below 17 K while the magnetic hyperfine field shows no reduction and is well represented by Eq. (5). This reduction of the muon precession frequency proves the microscopic coexistence of magnetic order and superconductivity and their competition. For comparison, the reduction of the muon spin frequency and therefore of the magnetic order parameter in $Ba_{1-x}Na_xFe_2As_2$ [30] is of the order of ≈65%. A description of this difference is given in Sec. III C. Possibly $B_{\rm hf}(T)$ shows no signatures for a reduction below 17 K since the reduction of 7% is within the hyperfine field error bars. Alternatively, the muon precession frequency may be reduced due to a spin reorientation below T_c rather than a reduction of the magnetic order parameter. However, in this scenario the angle θ between the magnetic hyperfine field $B_{\rm hf}$ and the principal axis of the EFG would change. The temperature dependence of θ is shown in Fig. 8. Since there is no systematic change of θ below T_c observed within error bars, a significant spin reorientation can be ruled out.

The critical exponent β can be estimated by setting $\alpha = 1$. The obtained values are shown in Table II. For $x = 0.35$, exponents of $\beta = 0.13(3)$ and 0.12(4) were obtained which are consistent with the two-dimensional (2D) Ising universality class ($\beta = 0.125$). This result is similar to undoped $BaFe_2As_2$ [34,35] as well as $Ba_{0.75}Na_{0.25}Fe_2As_2$ [30]. For $x = 0.50$, exponents of $\beta = 0.24(4)$ and 0.35(9) were obtained indicating a more three-dimensional behavior (3D Ising universality class: $\beta = 0.325$). The increase of the exponent β as a function of the Na-substitution level x indicates a tuning of the phase transition from first order for the undoped compound to second order for finite Na-substitution levels.

Low-temperature saturation values of the magnetic hyperfine field $B_{\rm hf}$, the muon spin precession frequency ν_A and θ, the angle between $B_{\rm hf}$ and the principal axis of the EFG, as a function of the Na-substitution level are summarized in Fig. 9. Upon Na substitution, a reduction of the magnetic hyperfine field and the muon spin precession frequency are observed, proving a reduction of the magnetic order parameter. The decrease in θ indicates a tilting of the magnetic moments out of the *ab* plane as a function of the Na-substitution level.

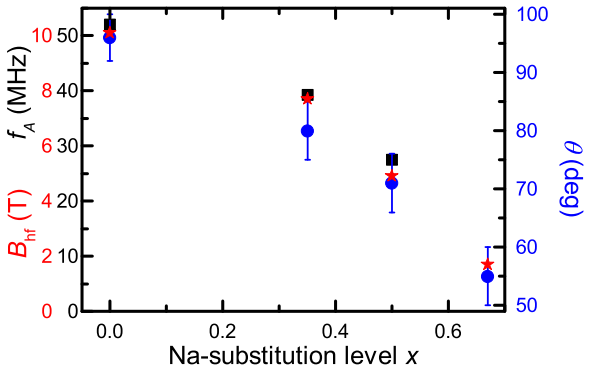

FIG. 9. (Color online) Low-temperature saturation values of the magnetic hyperfine field $B_{\rm hf}$, the muon spin precession frequency ν_A and θ, the angle between $B_{\rm hf}$ and the principal-axis of the EFG, as a function of the Na-substitution level. Upon Na substitution, a reduction of the magnetic hyperfine field and the muon spin precession frequency is observed, proving a reduction of the magnetic order parameter. The decrease in θ indicates a tilting of the magnetic moments out of the *ab* plane as a function of the Na-substitution level.

C. Landau theory for coupled order parameters: Coexistence of magnetic order and superconductivity

The 122 parent compounds $CaFe_2As_2$, $SrFe_2As_2$, and $BaFe_2As_2$ are multiband semimetals with five Fe 3*d* bands crossing the Fermi energy [8,23,36–38]. In the nonmagnetic state, two or more hole bands near (0,0) and two electron pockets near $(0,\pi)$ and $(\pi,0)$ cross the Fermi level in the unfolded Brillouin zone. Therefore, two electron and at least two hole Fermi surfaces (FS) are present. These multiple FSs with a high density of states at the FS enable various possibilities of electronic ordering, such as spin density wave (SDW), charge density wave (CDW), or superconductivity [5,39,40].

SDW order requires the presence of FS nesting. Angle-resolved photoemission spectroscopy (ARPES) experiments reveal a nonperfect FS nesting in the 122 parent compounds [41–43]. The electron pockets show an elliptical and the hole pockets a circular cross section [41–44]. Despite the different shapes of the pockets, there radii are of similar values in the undoped compounds and it is appropriate to speak of quasinesting [45]. By entering the SDW state below T_N, a reconstruction of the FS occurs as well as an opening of an electronic excitation gap at parts of the FS [46]. At the parts of the FS without a SDW gap, another state like SC or CDW may develop. In this itinerant description a coexistence of magnetism and superconductivity in real space is accompanied by a separation in momentum space.

Upon doping, the FSs may change. It was shown that the hole pocket expands and the electron pocket shrinks upon hole doping [47–49]. The size of the hole pockets at Γ increase due to the increased amount of holes per Fe, while the propeller blades of the electron pockets are reduced. This evolution reduces the quasinesting of the FSs and consequently weakens the SDW state.

It was shown by Fernandes *et al.* [6], Vorontsov *et al.* [5], and Schmiedt *et al.* [2] that a SDW can coexist with superconductivity. The result of their calculations is that a commensurate SDW can coexist with a superconducting $s^{\pm}$ state in a certain parameter range, if the electron pocket has a finite ellipticity and a difference in the chemical potentials of the electron and hole pockets is present.

In the case of coexistence of magnetic order and superconductivity, an interaction between both order parameters is

expected to be present. This may change the magnitude of the order parameters and alter the critical temperatures with respect to the decoupled situation. We have used a Landau theory to describe the coupling between the superconducting order parameter $\psi(\vec{r})$ and the magnetic order parameter $\vec{M}(\vec{r})$ in the case of coexistence and to describe the dependence of the reduction of the magnetic order parameter on the critical temperatures. The homogeneous free-energy functional in the absence of an external field is given by [4,40,50,51]

$$F[\psi,\vec{M}] = \int d^3r \left[\frac{\alpha}{2}|\psi(\vec{r})|^2 + \frac{\beta}{4}|\psi(\vec{r})|^4 + \frac{a}{2}|\vec{M}(\vec{r})|^2 + \frac{b}{4}|\vec{M}(\vec{r})|^4 + \frac{d}{2}|\psi(\vec{r})|^2|\vec{M}(\vec{r})|^2 \right], \tag{6}$$

where the coupling between the two order parameters is contained in the last term. Following the common approach, α and a are described as

$$a = a_0(T - T_{N0}), \tag{7}$$

$$\alpha = \alpha_0(T - T_{c0}), \tag{8}$$

where T_{N0} and T_{c0} denote the bare magnetic and superconducting transition temperatures, respectively. The bare transition temperatures describe the decoupled case. To ensure that the free energy has a minimum and that the two order parameters compete with each other, $\beta > 0, b > 0$, and $d > 0$ are required. The two order parameters are obtained by minimizing the free-energy functional $F[\psi,\vec{M}]$. The order parameters in the coexistence region are then given by

$$|\psi|^2 = -\frac{\alpha b - ad}{b\beta - d^2}, \quad \alpha b - ad < 0 \tag{9}$$

$$|\vec{M}|^2 = -\frac{a\beta - \alpha d}{b\beta - d^2}, \quad a\beta - \alpha d < 0. \tag{10}$$

This solution is stable for a sufficiently small coupling d, which satisfies $b\beta - d^2 > 0$. For the further treatment, $T_{c0} < T_{N0}$ is assumed, which is the case for sufficiently low doping in the 122 compounds. This results in $T_{N0} = T_N$. At T_c, where $|\psi|^2 = 0$, Eq. (9) reduces to

$$|\psi(T_c)|^2 = 0 = \alpha_0 b(T_c - T_{c0}) - a_0 d(T_c - T_N) \tag{11}$$

which results in a linear relation between the measured and bare superconducting transition temperatures. The temperature dependence of the magnetic order parameter in the coexistence regime is then given by

$$\vec{M}^2_{\mathrm{co}}(T) = \frac{1}{b\beta - d^2}\left\{ [\alpha_0 d - a_0\beta]T + \left[a_0\beta - \frac{a_0}{b}d^2\right]T_N - \left[1 - \frac{a_0 d}{\alpha_0 b}\right]T_c \right\}. \tag{12}$$

To investigate the reduction of the magnetic order parameter below the superconducting transition temperature, the ratio of $|\vec{M}_{\mathrm{co}}|^2(T)$ and $|\vec{M}_0|^2(T) = a_0(T_N - T)/b$ for $T < T_c$ is calculated. The reduction is maximal for $T \to 0$. The ratio is then given by

$$\frac{\vec{M}^2_{\mathrm{co}}}{\vec{M}^2_0}(T = 0) = 1 - \frac{d}{a_0}\frac{\alpha_0 b - a_0 d}{b\beta - d^2}\frac{T_c}{T_N}. \tag{13}$$

Literature data for $|\vec{M}_{\mathrm{co}}|^2/|\vec{M}_0|^2(T = 0)$ as a function of T_c/T_N for various 122 compounds, measured by neutron scattering and μSR [27,30,52–61] as well as the reduction of the structural order parameter $S = (a_c - b_c)/(a_c + b_c)$ (with a_c and b_c being the crystallographic a and b axis parameters, respectively) are shown in Fig. 10.

The reduction of the magnetic and structural order parameters shows the same behavior supporting the idea of a strong magnetoelastic coupling in the 122 pnictides [21,29,32,53,62–67]. The linearity of $M \propto S$, as it was seen, e.g., in several 122 compounds [21,32,45,62] requires a biquadratic coupling ($\propto S^2M^2$) between both order parameters showing that both order parameters are on equal terms.

$|\vec{M}_{\mathrm{co}}|^2/|\vec{M}_0|^2(T = 0)$ shows a nearly linear decrease as a function of T_c/T_N and hence the reduction of the magnetic order parameter shows a square-root behavior. This corresponds to a constant slope in Eq. (13), which implies a similar coupling strength of the magnetic and superconducting order parameters in the 122 compounds. For $T_c/T_N \ll 1$, experimental data show no reduction of the magnetic order parameter in the coexistence regime. This may result from the fact that the samples show SC only in parts of the sample volume, which has been observed for, e.g., $Ca_{0.65}Na_{0.35}Fe_2As_2$. Equation (13) qualitatively describes the reduction of $|\vec{M}_{\mathrm{co}}|^2/|\vec{M}_0|^2(T = 0)$ with increasing T_c/T_N ratio for $0 < T_c/T_N < 0.7$. The systematic deviations for $T_c/T_N > 0.7$ indicate an increase in the coupling strength. This means that the coupling is more effective if $T_c \approx T_N$. This implies that the superconductivity removes more electronic states from the FS and consequently weakens the magnetic order parameter.

The Landau theory qualitatively describes the reduction of the magnetic order parameter in the coexistence phase. The phenomenological functional in Eq. (6) with lowest-order temperature dependencies of the parameters a, b, α, and β does not permit a quantitative description for $T \to 0$. This could be improved by expanding to higher orders in the order parameters and calculating the parameters from microscopic theory. On the other hand, mean-field approximation itself should be valid outside of the critical regime, where we experimentally find Ising critical behavior (see Sec. III B). We thus expect the mean-field approximation to hold for $T \to 0$.

D. Lattice dynamics and chemical shift changes at the magnetostructural phase transition

The lattice dynamics of $Ca_{1-x}Na_xFe_2As_2$ was investigated by analyzing the temperature dependence of the Mössbauer-Lamb factor. The recoilless fraction f was extracted from the Mössbauer spectra using the absorption area method [68]. In the Debye-approximation [69]

$$f \propto \exp\left\{ -\frac{3E_R}{2k_B\theta_D}\left[1 + 4\left(\frac{T}{\theta_D}\right)^2 \int_0^{\theta_D/T} \frac{x}{e^x - 1}dx \right] \right\}, \tag{14}$$

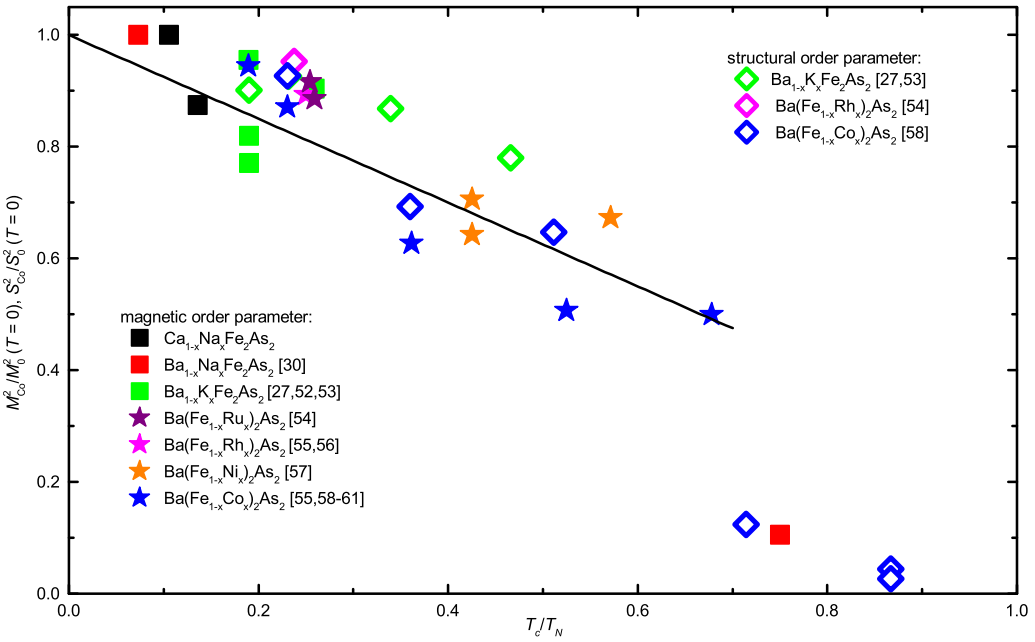

FIG. 10. (Color online) $|\vec{M}_{\rm co}|^2/|\vec{M}_0|^2(T=0)$ as a function of T_c/T_N for various 122 compounds [27,30,52–61]. $|\vec{M}_{\rm co}|^2$ denotes the magnetic order parameter in the region of coexistence with superconductivity. $|\vec{M}_0|^2$ denotes the magnetic order parameter without any superconductivity. The reduction of the magnetic order parameter in the coexistence region increases with increase of T_c/T_N following Eq. (13), the best linear fit for $T < 0.7$ is shown as the solid line. Error bars are below the size of the dots. Data taken from $Ba_{1-x}Na_xFe_2As_2$ [30], $Ba_{1-x}K_xFe_2As_2$ [27,52,53], $Ba(Fe_{1-x}Ru_x)_2As_2$ [54], $Ba(Fe_{1-x}Rh_x)_2As_2$ [55,56], $Ba(Fe_{1-x}Ni_x)_2As_2$ [57], and $Ba(Fe_{1-x}Co_x)_2As_2$ [55,58–61].

with Boltzmann constant k_B, Debye temperature θ_D, and the recoil energy E_R. The temperature dependence of the relative recoilless fraction $f(T)/f(4.2\ \mathrm{K})$ is shown in Fig. 11. The data for temperatures above and below the phase transition were analyzed using Eq. (14) to investigate the influence of the magnetic phase transition on f. We accordingly define Debye temperatures $\theta_D^{\rm PM}$ and $\theta_D^{\rm AFM}$. The step at 151 K for $x = 0.35$ and the gradual increase between 60 and 125 K for $x = 0.50$ are attributed to an effective absorber-thickness effect. The magnetic phase transition leads to an increase of the absorption area compared to the paramagnetic region, due to a splitting of the resonance lines [69,70]. The obtained Debye temperatures are shown in Table III. As the Debye temperatures $\theta_D^{\rm PM}$ and $\theta_D^{\rm AFM}$ do not change significantly within error bars at the phase transition, we conclude that the lattice dynamics does not change upon the magnetostructural phase transition. For $x = 0.00$ and 0.33, $\theta_D = 241$–292 K [71–75] and $\theta_D = 217$ K [9], respectively, were reported. This reduction in θ_D can be associated with the increasing volume of the unit cell as a function of x. Our measurements show that the Debye temperature is constant within error bars in the Na-substitution level range $0.35 \leqslant x \leqslant 0.67$ showing that the lattice dynamics are independent of x. This indicates that the Na substitution in the alkaline-earth layer does not affect the vibration modes of the Fe atoms within the resolution of Mössbauer spectroscopy. It should be noted that Mössbauer spectroscopy only probes the phonon spectra of the Fe atoms, while specific-heat measurements

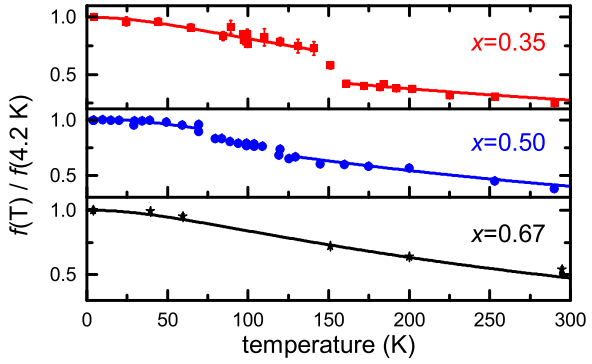

FIG. 11. (Color online) Temperature dependence of the relative recoilless fraction $f(T)/f(4.2\ \mathrm{K})$ including fits following Eq. (14).

TABLE III. Debye temperatures θ_D extracted from the temperature dependence of the Debye-Waller factor using Eq. (14) above (PM) and below (AFM) the magnetic phase transition. Literature specific-heat results for the Debye temperature are shown for comparison.

x	$\theta_D^{\rm PM}$/K	$\theta_D^{\rm AFM}$/K
0.00	272 [71]	271 [71]
0.35	200(32)	208(16)
0.50	203(12)	219(28)
0.67	213(6)	
	Literature specific-heat results	
0.00	258 [72]	
0.00	292 [73]	
0.00	267 [74]	
0.00	241 [75]	
0.33	217 [76]	
0.68	267 [9]	

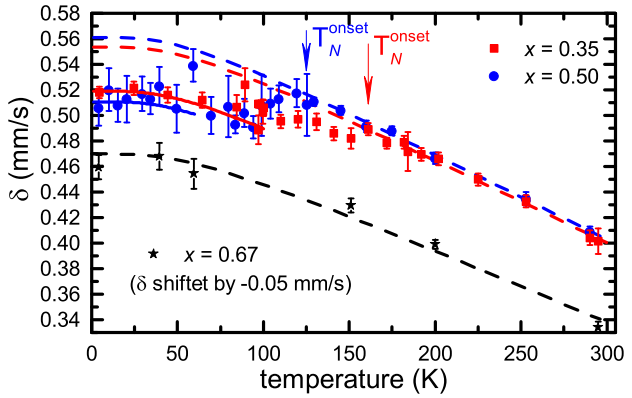

FIG. 12. (Color online) Temperature dependence of the isomer shift. The dashed (solid) lines are a fit in the paramagnetic (magnetically ordered) temperature regime using Eq. (15) with θ_D = 200, 203, and 213 K for $x = 0.35$, 0.50, and 0.67, respectively, leading to $\delta^{\mathrm{PM}}(T)$. The deviation from $\delta^{\mathrm{PM}}(T)$ corresponds to the magnetostructural phase transition, which causes a change in the electron density at the nucleus. Data and fit for $x = 0.67$ are shifted by $\delta = -0.05$ mm/s for clarity.

probe the phonon spectra of the whole lattice. In particular, we probe the vibrations of the Fe atoms parallel to the crystallographic c axis as the single crystals are aligned with the ab plane perpendicular to the γ beam direction. This may explain the difference in θ_D for $x = 0.67$ and 0.68 obtained by Mössbauer spectroscopy and specific-heat measurements, respectively.

To further study the electromagnetic properties at the magnetostructural phase transition, the temperature dependence of the isomer shift δ was analyzed. δ is a measure for the electron density at the Fe nucleus. The temperature dependence of the isomer shift [69], which is shown in Fig. 12, is a sum of the temperature-independent chemical shift δ_c and a temperature-dependent contribution $\delta_{\mathrm{R}}(T)$ due to the second-order Doppler shift

$$\delta(T) = \delta_c + \delta_{\mathrm{R}}(T), \tag{15}$$

$$\delta_R(T) = -\frac{9}{16}\frac{k_B}{M_{\mathrm{eff}}\mathrm{c}}\left[\theta_D + 8T\left(\frac{T}{\theta_D}\right)^3 \int_0^{\theta_D/T} \frac{x^3}{e^x - 1}\mathrm{d}x\right], \tag{16}$$

where M_{eff} denotes the effective mass of the ^{57}Fe atom. δ_c can be calculated using $\delta_c = \delta(0) - \delta_{\mathrm{R}}(0)$. To study the influence of the magnetostructural phase transition on the isomer shift, the temperature dependence of the isomer shift was analyzed in the following way: $\delta(T)$ was analyzed in the paramagnetic state with a fixed θ_D, obtained from Eq. (14). Then, we extracted the temperature dependence from $\delta^{\mathrm{PM}}(T)$. In a third step, we have checked whether $\delta^{\mathrm{PM}}(T)$ can describe the temperature dependence of the isomer shift in the magnetically ordered state or whether systematic deviations from the behavior in the paramagnetic state occur. $\delta^{\mathrm{PM}}(T)$ reveals similar behavior for both samples with $x = 0.35$ and 0.50 leading to $\delta_c^{\mathrm{PM}} = 0.61(3)$ mm/s and $\delta_c^{\mathrm{PM}} = 0.60(1)$ mm/s. For $x = 0.35$, below the onset of the magnetic order, a deviation from the paramagnetic behavior is found. δ_c^{PM} is reduced to a value of $\delta_c^{\mathrm{AFM}} = 0.57(1)$ mm/s. For $x = 0.50$, a reduction to a value of $\delta_c^{\mathrm{AFM}} = 0.56(1)$ mm/s was observed. Also, this reduction occurs over a wider temperature range as the magnetic transition is broader.

These reductions in the chemical shifts correspond to an increase in the electron density at the nucleus [69]. The origin of this increase can be the structural or the magnetic phase transition. In metallic iron at the Curie temperature, for example, a reduction of δ_c of $\approx$0.3 mm/s was observed [77]. In nonmagnetic FeSe, for example, an increase in δ_c of 0.006(1) mm/s at the tetragonal-to-orthorhombic phase transition was observed [78]. The change from a tetragonal to an orthorhombic structure changes the lattice parameters and hence the volume of the unit cell, which changes the chemical shift [69]. An increase of the volume and hence an increase of the Fe-As distance results in an decrease of the electron density at the nucleus corresponding to an increased δ_c [71]. Therefore, the change of the chemical shifts is caused by the magnetostructural phase transition, where the structural changes result in an increase of δ_c [71,78]. But, as δ_c is reduced at the magnetostructural phase transition, the magnetic ordering has to reduce δ_c. It should be noted that previous Mössbauer measurements on the undoped compound show contradicting results with either no change [20], an increase [71], or a decrease [79] in the chemical shift.

For $x = 0.67$, the temperature dependence of $\delta(T)$ can be properly described by Eq. (15) and a value of δ_c = 0.56(1) mm/s was obtained. Therefore, no signs of a magnetic or structural phase transition were found.

E. Superconductivity in optimal doped $Ca_{0.33}Na_{0.67}Fe_2As_2$

For $Ca_{0.33}Na_{0.67}Fe_2As_2$ ($x = 0.67$), susceptibility measurements evidence bulk superconductivity below $T_c = 34$ K, as shown in Fig. 3. Mössbauer spectra down to 5 K are shown in Fig. 7. Above 151 K, a doublet structure with V_{zz}= 10.3(2) V/Å^2 is observed. This is consistent with a pure paramagnetic phase. V_{zz} is constant within error bars down to lowest temperatures indicating the absence of a structural phase transition. Below 60 K, a broadening of the spectra is observed. This broadening indicates small magnetic fields, which were modeled using a Gaussian distribution with a first moment $\langle B \rangle = 0$. The standard deviation of this Gaussian distribution is constant within error bars, $\sigma(B)$ = 2.2(1) T, above T_c and decreases in the superconducting phase to 1.7(1) T at 4.2 K. This indicates a competition between magnetism and superconductivity. Additionally, the spectra are nearly symmetric below 60 K and an angle θ = 55(5)° between the principal axis of the EFG and the magnetic hyperfine field is obtained, which is close to the magic angle. ZF μSR experiments down to 5 K are shown in Fig. 4. The time evolution of the muon spin polarization exhibits a Gauss-Kubo-Toyabe depolarization above 75 K excluding any electronic magnetic order. Below 40 K, a weak exponential relaxation supports short-range magnetic order in a small volume fraction with a MVF smaller than 20%. By combining both local probes, the onset temperature of the weak magnetic order is estimated to be 60 K $< T_N^{\mathrm{onset}} <$ 75 K. However, room-temperature Mössbauer measurements as well as the sharp superconducting transition observed by

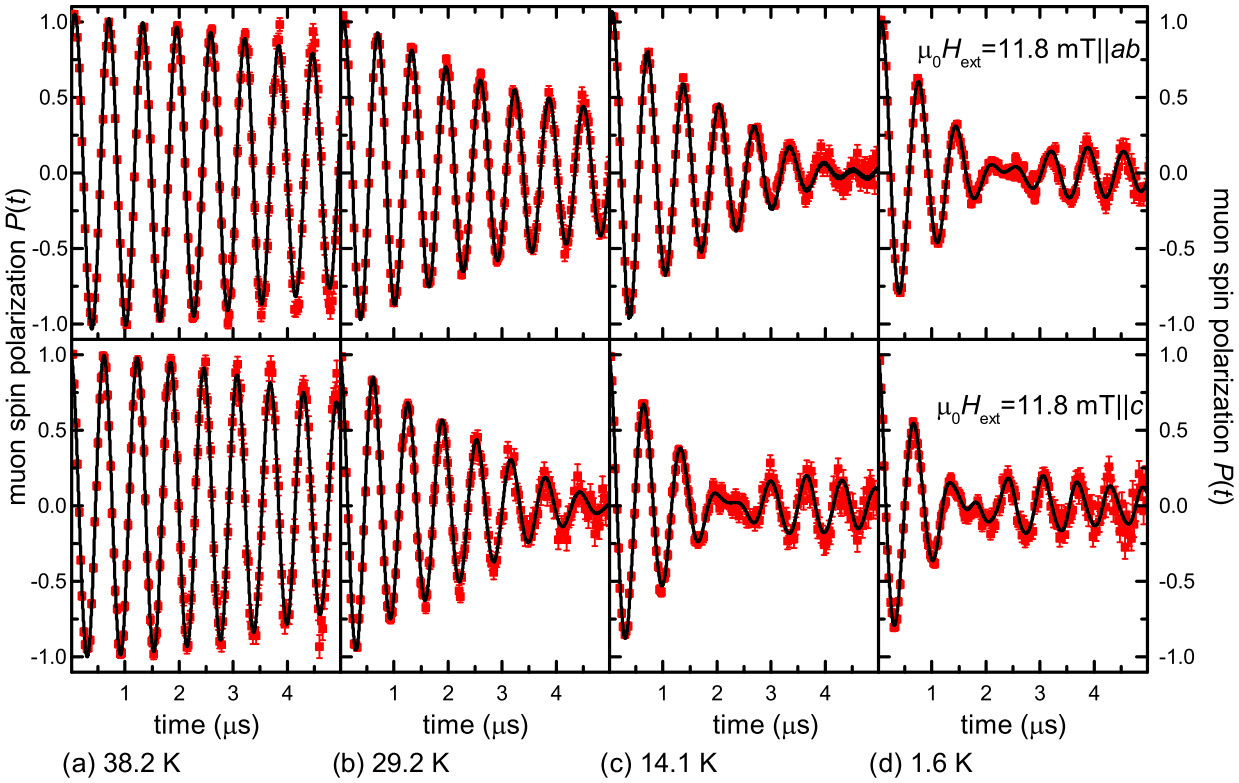

FIG. 13. (Color online) TF μSR spectra for $x = 0.67$ with $\mu_0 H_{\rm ext} = 11.8$ mT $\parallel ab$ (upper row) and $\mu_0 H_{\rm ext}$=11.8 mT $\parallel c$ (lower row) for temperatures above and below the superconducting transition temperature $T_c = 34$ K. The small (Gaussian) damping in spectrum (a) is attributed to the dipolar interaction of the muon spin with randomly distributed nuclear moments. The additional damping in spectra (b)–(d) is caused by the formation of the vortex lattice in the superconducting state and the associated internal magnetic field distribution $n(B)$. It is clearly visible that the damping of the muon precession is stronger in the case $\mu_0 H_{\rm ext} = 11.8$ mT $\parallel c$.

magnetic susceptibility measurements confirm a homogeneous sample. This indicates that the weak magnetism is diluted and disordered and persistent even in the optimal doping regime, similar to other iron pnictides [82–84].

For an investigation of the superconducting phase, TF μSR measurements were performed in external magnetic fields of $\mu_0 H_{\rm ext} = 11.8$ mT perpendicular and parallel to the crystallographic c axis. The magnetic field was applied at $T > T_c$ and the corresponding muon spin polarization is shown in Fig. 13(a). The weak relaxation above T_c is caused by the dipole-dipole interaction of the muon spin with randomly distributed dense nuclear moments. Additional damping is found in the case of a type-II superconductor for $\mu_0 H_{c1} < \mu_0 H_{\rm ext} < \mu_0 H_{c2}$ due to the vortex lattice formation. The effect of the vortex lattice on the muon spin polarization is shown in Figs. 13(b)–13(d). The superconducting signal fraction is fully damped after a few μs and $\approx$18% residual signal fraction is still oscillating with a precession frequency equal to the applied field at times $t > 3$ μs. Identifying this $\approx$18% signal fraction with the MVF obtained by ZF μSR measurements, which is of equal value, shows that the internal magnetic fields are small compared to the 11.8 mT applied field.

The London penetration depth can be obtained by measuring the magnetic-field distribution within the vortex lattice and employing Eq. (4). Using the measurements with $\mu_0 H_{\rm ext} \parallel c$, the in-plane penetration depth λ_{ab} can be directly calculated. For $\mu_0 H_{\rm ext} \perp c$, contributions from λ_{ac} and λ_{bc} are measured, resulting in an effective magnetic penetration depth $\lambda_{c_{\rm eff}}$. Under the assumption of $\lambda_a \approx \lambda_b$, a value for λ_c can be estimated using [85]

$$\lambda_{ab} = \sqrt{\lambda_a \lambda_b} \approx \lambda_a \rightarrow \lambda_{c_{\rm eff}} = \sqrt{\lambda_a \lambda_c} \rightarrow \lambda_c = \frac{\lambda_{c_{\rm eff}}^2}{\lambda_a}. \quad (17)$$

The resulting temperature dependence of the inverse squared London penetration depth $\lambda_{ab}^{-2}(T)$ and $\lambda_c^{-2}(T)$ is shown in Figs. 14(a) and 14(b), respectively, together with the average internal field $\langle B \rangle$, which shows a reduction due to the diamagnetic shielding below the superconducting transition. $\lambda^{-2}(T)$ was modeled using the phenomenological α model including two independent superconducting gaps with s-wave symmetry and a fixed $T_c = 34$ K [80]. The results are shown in Table IV as well as results of ARPES [47] ($x = 0.67$) and specific-heat measurements [9] ($x = 0.68$) on single crystals. Disorder in the vortex lattice would artificially reduce the magnetic penetration depth due to the broadening of $n(B)$. For this reason, λ_{ab} and λ_c strictly describe lower limits (and λ^{-2} an upper limit). Therefore, the obtained values for the magnetic penetration depths are reduced compared to the values obtained by, e.g., specific-heat measurements. To illustrate this effect, the temperature dependence of $\lambda_{\rm spec.\ heat}^{-2}(T)$ with the corresponding parameter [$\Delta_1 = 2.35$ meV, $\Delta_2 = 7.5$ meV, $W(\Delta_1) = 0.75$, and $\lambda(0) = 210$ nm] obtained by specific-heat

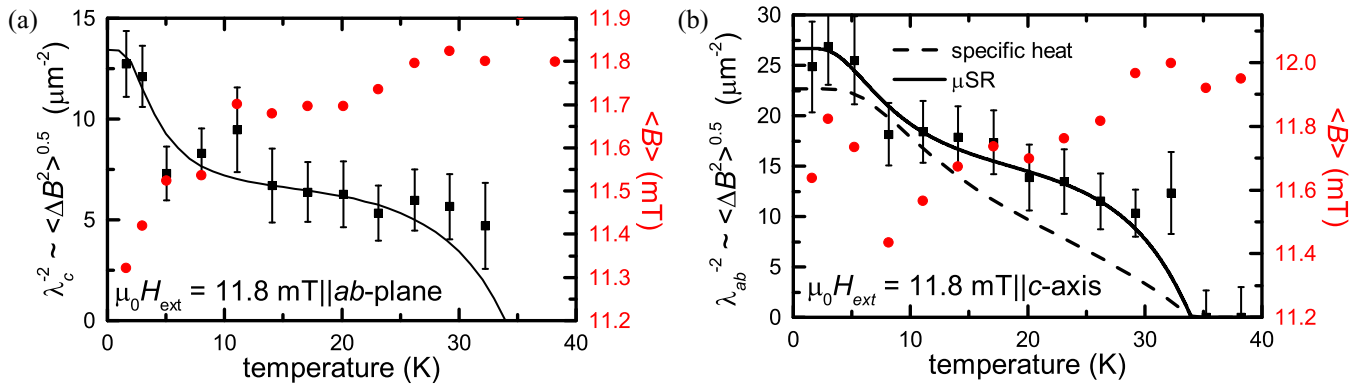

FIG. 14. (Color online) Temperature dependence of the magnetic penetration depth (a) $\lambda_c^{-2}(T)$ and (b) $\lambda_{ab}^{-2}(T)$ (proportional to the superfluid density) after field cooling in $\mu_0 H = 11.8$ mT, including the fit (solid lines) with a phenomenological α model [80], and the average magnetic field determined by TF μSR. The dashed curve in (b) displays the temperature dependence of λ^{-2} with gap values of $\Delta_1 = 2.35$ meV, $\Delta_2 = 7.5$ meV, $W(\Delta_1) = 0.75$, and $\lambda(0) = 210$ nm, obtained by specific-heat measurements [9,81]. The reduction of the average magnetic field is caused by the diamagnetic shielding of the superconducting phase. The measurements were performed at a sample with $x = 0.67$.

measurements [9,81] is plotted in Fig. 14(b). It is clearly visible that $\lambda^{-2}_{\text{spec. heat}}(T) < \lambda^{-2}_{\mu\text{SR}}(T)$ for $T < T_c$. This underestimation of the magnetic penetration depth in the μSR experiments may result in a different temperature dependence of $\lambda^{-2}(T)$ and therefore in different gap sizes and weighting factors. Additionally, Johnston *et al.* considered the interband coupling of the superconducting bands and found an intermediate coupling strength [9]. The α-model used in this work considers two noninteracting superconducting bands, which may also explain the different parameter values. Taking into account the accuracy of magnetic penetration depth measurements by means of the μSR experiments using the α model, the obtained parameter for $\Delta_1(0)$, $\Delta_2(0)$, $W(\Delta_1)$, and $\lambda(0)$ are in good agreement with the values obtained by ARPES and specific-heat experiments [9,47,81].

The anisotropy of the magnetic penetration can be calculated by under the assumption that $\lambda_a \approx \lambda_b$ by [85]

$$\gamma_\lambda = \frac{\lambda_c}{\lambda_{ab}}. \tag{18}$$

A temperature-independent value of $\gamma_\lambda = 1.5(4)$ is the smallest observed among the 122 pnictides indicating a more 3D behavior [9]. This behavior is consistent with the temperature-independent value of $\gamma = 1.85(5)$ for the anisotropy of the upper critical fields [86].

TABLE IV. Values of the superconducting gap and the magnetic penetration depth obtained by a phenomenological α-model analysis of $\lambda_c^{-2}(T)$ and $\lambda_{ab}^{-2}(T)$. $\Delta_i(0)$ denotes the zero-temperature values of the gaps. $W(\Delta_1)$ and $W(\Delta_2) = 1 - W(\Delta_1)$ are the corresponding weighting factors. $\lambda(0)$ denotes the zero-temperature penetration depth. The here presented μSR as well as the ARPES measurements were performed on samples with $x = 0.67$ while the specfic-heat measurements were performed at samples with $x = 0.68$.

	$\Delta_1(0)$/meV	$\Delta_2(0)$/meV	$W(\Delta_1)$	$\lambda(0)$/nm
λ_c	0.57(8)	6.7(1.3)	0.49(4)	280(46)
λ_{ab}	0.8(3)	6(1)	0.46(8)	194(17)
ARPES [47]	2.3	7.8		
Spec. heat [9,81]	2.35	7.5	0.75 [9]	210(10) [81]

IV. SUMMARY AND CONCLUSIONS

In summary, we performed muon spin relaxation and Mössbauer experiments on $Ca_{1-x}Na_xFe_2As_2$ single crystals with $x = 0.00$, 0.35, 0.50, and 0.67 resulting in an updated phase diagram, which is shown in Fig. 1. The substitution of Ca by Na reduces the onset of the magnetic ordering from $T_N^{\text{onset}} = 167(2)$ to 161(2) and 125(3) K while the magnetic phase transition temperature width $\Delta T = T_N^{\text{onset}} - T_N^{100\%}$ increases from 4 to 21 and 45 K for $x = 0.00$, 0.35, and 0.50, respectively. The muon spin precession frequency ν as well as the magnetic hyperfine field B_{hf}, which are proportional to the magnetic order parameter, are reduced as a function of the Na-substitution level. Both μSR as well as Mössbauer spectroscopy indicate an increased tilting of the magnetic structure upon doping. The lattice dynamics does not change at the magnetostructural phase transition. Magnetic susceptibility measurements indicate superconductivity in parts of the sample volume for $x = 0.35$, whereas the sample with $x = 0.50$ shows bulk superconductivity. Therefore, as 100% of the sample is magnetically ordered, coexistence of magnetic order and superconductivity in parts ($x = 0.35$) or in the whole sample ($x = 0.50$) was observed. A strong reduction of the magnetic order parameter, as found in the $Ba_{1-x}Na_xFe_2As_2$ series [30], is not observed for $Ca_{1-x}Na_xFe_2As_2$ with $x = 0.35$. For $x = 0.50$, a small reduction of $\approx$7% was observed. We applied a Landau theory to describe the reduction of the magnetic order parameter showing that the magnitude of the reduction depends on the coupling strength and the T_c/T_N ratio. A linear relation between the reduction of $|\vec{M}_{\text{co}}|^2/|\vec{M}_0|^2(T = 0)$ on T_c/T_N has been found for several superconducting 122-pnictide systems that shows microscopic coexistence.

For $x = 0.67$, diluted and weak magnetism below 60–75 K as well as bulk superconductivity with $T_c = 34$ K is found. The s-wave symmetry of the two superconducting gaps as well as the value of the larger gap agrees well with recent ARPES and specific-heat measurements [47,87].

ACKNOWLEDGMENTS

This work was funded by the German Science Foundation (DFG) within the research training group GRK 1621 as well as under the Projects No. WU595/3-1 (S.W.), No. BE1749/13 and No. BU887/15-1 (B.B.), and No. SA 2426/1-1 (R.S.). The authors would like to thank S.-L. Drechsler, IFW Dresden, for valuable discussions. Part of this work was performed at the Swiss Muon Source at the Paul Scherrer Institute, Switzerland.

[1] Y. Kamihara, T. Watanabe, M. Hirano, and H. Hosono, J. Am. Chem. Soc. **130**, 3296 (2008).
[2] J. Schmiedt, P. M. R. Brydon, and C. Timm, Phys. Rev. B **89**, 054515 (2014).
[3] D. Parker, M. G. Vavilov, A. V. Chubukov, and I. I. Mazin, Phys. Rev. B **80**, 100508 (2009).
[4] R. M. Fernandes and J. Schmalian, Phys. Rev. B **82**, 014521 (2010).
[5] A. B. Vorontsov, M. G. Vavilov, and A. V. Chubukov, Phys. Rev. B **81**, 174538 (2010).
[6] R. M. Fernandes, D. K. Pratt, W. Tian, J. Zarestky, A. Kreyssig, S. Nandi, M. G. Kim, A. Thaler, N. Ni, P. C. Canfield, R. J. McQueeney, J. Schmalian, and A. I. Goldman, Phys. Rev. B **81**, 140501 (2010).
[7] K. Zhao, Q. Q. Liu, X. C. Wang, Z. Deng, Y. X. Lv, J. L. Zhu, F. Y. Li, and C. Q. Jin, Phys. Rev. B **84**, 184534 (2011).
[8] G. Wu, H. Chen, T. Wu, Y. L. Xie, Y. J. Yan, R. H. Liu, X. F. Wang, J. J. Ying, and X. H. Chen, J. Phys.: Condens. Matter **20**, 422201 (2008).
[9] S. Johnston, M. Abdel-Hafiez, L. Harnagea, V. Grinenko, D. Bombor, Y. Krupskaya, C. Hess, S. Wurmehl, A. U. B. Wolter, B. Büchner, H. Rosner, and S.-L. Drechsler, Phys. Rev. B **89**, 134507 (2014).
[10] A. Suter and B. Wojek, Phys. Procedia **30**, 69 (2012).
[11] P. D. de Réotier and A. Yaouanc, J. Phys.: Condens. Matter **9**, 9113 (1997).
[12] A. Yaouanc and P. de Réotier, *Muon Spin Rotation, Relaxation, and Resonance: Applications to Condensed Matter*, International Series of Monographs on Physics (Oxford University Press, Oxford, 2011).
[13] A. Maisuradze, R. Khasanov, A. Shengelaya, and H. Keller, J. Phys.: Condens. Matter **21**, 075701 (2009).
[14] E. H. Brandt, Phys. Rev. B **37**, 2349 (1988).
[15] L. Harnagea, S. Singh, G. Friemel, N. Leps, D. Bombor, M. Abdel-Hafiez, A. U. B. Wolter, C. Hess, R. Klingeler, G. Behr, S. Wurmehl, and B. Büchner, Phys. Rev. B **83**, 094523 (2011).
[16] S. Aswartham, M. Abdel-Hafiez, D. Bombor, M. Kumar, A. U. B. Wolter, C. Hess, D. V. Evtushinsky, V. B. Zabolotnyy, A. A. Kordyuk, T. K. Kim, S. V. Borisenko, G. Behr, B. Büchner, and S. Wurmehl, Phys. Rev. B **85**, 224520 (2012).
[17] R. Klingeler, N. Leps, I. Hellmann, A. Popa, U. Stockert, C. Hess, V. Kataev, H.-J. Grafe, F. Hammerath, G. Lang, S. Wurmehl, G. Behr, L. Harnagea, S. Singh, and B. Büchner, Phys. Rev. B **81**, 024506 (2010).
[18] G. M. Zhang, Y. H. Su, Z. Y. Lu, Z. Y. Weng, D. H. Lee, and T. Xiang, Europhys. Lett. **86**, 37006 (2009).
[19] A. A. Aczel, E. Baggio-Saitovitch, S. L. Budko, P. C. Canfield, J. P. Carlo, G. F. Chen, P. Dai, T. Goko, W. Z. Hu, G. M. Luke, J. L. Luo, N. Ni, D. R. Sanchez-Candela, F. F. Tafti, N. L. Wang, T. J. Williams, W. Yu, and Y. J. Uemura, Phys. Rev. B **78**, 214503 (2008).
[20] M. Alzamora, J. Munevar, E. Baggio-Saitovitch, S. L. Bud'ko, N. Ni, P. C. Canfield, and D. R. Sánchez, J. Phys.: Condens. Matter **23**, 145701 (2011).
[21] A. Jesche, N. Caroca-Canales, H. Rosner, H. Borrmann, A. Ormeci, D. Kasinathan, H. H. Klauss, H. Luetkens, R. Khasanov, A. Amato, A. Hoser, K. Kaneko, C. Krellner, and C. Geibel, Phys. Rev. B **78**, 180504 (2008).
[22] M. Tegel, M. Rotter, V. Weiß, F. M. Schappacher, R. Pöttgen, and D. Johrendt, J. Phys.: Condens. Matter **20**, 452201 (2008).
[23] M. Rotter, M. Tegel, D. Johrendt, I. Schellenberg, W. Hermes, and R. Pöttgen, Phys. Rev. B **78**, 020503 (2008).
[24] R. D. Shannon, Acta Crystallogr., Sec. A **32**, 751 (1976).
[25] H.-H. Klauss, H. Luetkens, R. Klingeler, C. Hess, F. J. Litterst, M. Kraken, M. M. Korshunov, I. Eremin, S.-L. Drechsler, R. Khasanov, A. Amato, J. Hamann-Borrero, N. Leps, A. Kondrat, G. Behr, J. Werner, and B. Büchner, Phys. Rev. Lett. **101**, 077005 (2008).
[26] A. Amato, R. Khasanov, H. Luetkens, and H.-H. Klauss, Phys. C (Amsterdam) **469**, 606 (2009).
[27] E. Wiesenmayer, H. Luetkens, G. Pascua, R. Khasanov, A. Amato, H. Potts, B. Banusch, H.-H. Klauss, and D. Johrendt, Phys. Rev. Lett. **107**, 237001 (2011).
[28] M. Rotter, M. Pangerl, M. Tegel, and D. Johrendt, Angew. Chem. Int. Ed. **47**, 7949 (2008).
[29] A. I. Goldman, D. N. Argyriou, B. Ouladdiaf, T. Chatterji, A. Kreyssig, S. Nandi, N. Ni, S. L. Bud'ko, P. C. Canfield, and R. J. McQueeney, Phys. Rev. B **78**, 100506 (2008).
[30] H. Maeter, G. Pascua, H. Luetkens, J. Knolle, S. Aswartham, S. Wurmehl, G. Behr, B. Büchner, Z. Shermadini, K. Sedlak, A. Amato, R. Moessner, I. Eremin,, and H.-H. Klauss, arXiv:1210.6881v1.
[31] T. Goko, A. A. Aczel, E. Baggio-Saitovitch, S. L. Bud'ko, P. C. Canfield, J. P. Carlo, G. F. Chen, P. Dai, A. C. Hamann, W. Z. Hu, H. Kageyama, G. M. Luke, J. L. Luo, B. Nachumi, N. Ni, D. Reznik, D. R. Sanchez-Candela, A. T. Savici, K. J. Sikes, N. L. Wang, C. R. Wiebe, T. J. Williams, T. Yamamoto, W. Yu, and Y. J. Uemura, Phys. Rev. B **80**, 024508 (2009).
[32] S. Avci, J. M. Allred, O. Chmaissem, D. Y. Chung, S. Rosenkranz, J. A. Schlueter, H. Claus, A. Daoud-Aladine, D. D. Khalyavin, P. Manuel, A. Llobet, M. R. Suchomel, M. G. Kanatzidis, and R. Osborn, Phys. Rev. B **88**, 094510 (2013).
[33] R. Cortes-Gil and S. J. Clarke, Chem. Mater. **23**, 1009 (2011).
[34] S. D. Wilson, C. R. Rotundu, Z. Yamani, P. N. Valdivia, B. Freelon, E. Bourret-Courchesne, and R. J. Birgeneau, Phys. Rev. B **81**, 014501 (2010).
[35] S. D. Wilson, Z. Yamani, C. R. Rotundu, B. Freelon, E. Bourret-Courchesne, and R. J. Birgeneau, Phys. Rev. B **79**, 184519 (2009).
[36] G. F. Chen, Z. Li, J. Dong, G. Li, W. Z. Hu, X. D. Zhang, X. H. Song, P. Zheng, N. L. Wang, and J. L. Luo, Phys. Rev. B **78**, 224512 (2008).

[37] P. J. Hirschfeld, M. M. Korshunov, and I. I. Mazin, Rep. Prog. Phys. **74**, 124508 (2011).

[38] D. Johrendt, J. Mater. Chem. **21**, 13726 (2011).

[39] D. Singh, Phys. C (Amsterdam) **469**, 418 (2009).

[40] M. G. Vavilov, A. V. Chubukov, and A. B. Vorontsov, Supercond. Sci. Technol. **23**, 054011 (2010).

[41] G. Liu, H. Liu, L. Zhao, W. Zhang, X. Jia, J. Meng, X. Dong, J. Zhang, G. F. Chen, G. Wang, Y. Zhou, Y. Zhu, X. Wang, Z. Xu, C. Chen, and X. J. Zhou, Phys. Rev. B **80**, 134519 (2009).

[42] M. Neupane, P. Richard, Y.-M. Xu, K. Nakayama, T. Sato, T. Takahashi, A. V. Federov, G. Xu, X. Dai, Z. Fang, Z. Wang, G.-F. Chen, N.-L. Wang, H.-H. Wen, and H. Ding, Phys. Rev. B **83**, 094522 (2011).

[43] C. Liu, T. Kondo, N. Ni, A. D. Palczewski, A. Bostwick, G. D. Samolyuk, R. Khasanov, M. Shi, E. Rotenberg, S. L. Bud'ko, P. C. Canfield, and A. Kaminski, Phys. Rev. Lett. **102**, 167004 (2009).

[44] R. Gonnelli, M. Tortello, D. Daghero, P. Pecchio, S. Galasso, V. Stepanov, Z. Bukowski, N. Zhigadlo, J. Karpinski, K. Iida, and B. Holzapfel, J. Supercond. **26**, 1331 (2013).

[45] S. Avci, O. Chmaissem, D. Y. Chung, S. Rosenkranz, E. A. Goremychkin, J. P. Castellan, I. S. Todorov, J. A. Schlueter, H. Claus, A. Daoud-Aladine, D. D. Khalyavin, M. G. Kanatzidis, and R. Osborn, Phys. Rev. B **85**, 184507 (2012).

[46] T. Kondo, R. M. Fernandes, R. Khasanov, C. Liu, A. D. Palczewski, N. Ni, M. Shi, A. Bostwick, E. Rotenberg, J. Schmalian, S. L. Bud'ko, P. C. Canfield, and A. Kaminski, Phys. Rev. B **81**, 060507 (2010).

[47] D. V. Evtushinsky, V. B. Zabolotnyy, L. Harnagea, A. N. Yaresko, S. Thirupathaiah, A. A. Kordyuk, J. Maletz, S. Aswartham, S. Wurmehl, E. Rienks, R. Follath, B. Büchner, and S. V. Borisenko, Phys. Rev. B **87**, 094501 (2013).

[48] D. V. Evtushinsky, D. S. Inosov, V. B. Zabolotnyy, M. S. Viazovska, R. Khasanov, A. Amato, H.-H. Klauss, H. Luetkens, C. Niedermayer, G. L. Sun, V. Hinkov, C. T. Lin, A. Varykhalov, A. Koitzsch, M. Knupfer, B. Büchner, A. A. Kordyuk, and S. V. Borisenko, New J. Phys. **11**, 055069 (2009).

[49] C. Liu, G. D. Samolyuk, Y. Lee, N. Ni, T. Kondo, A. F. Santander-Syro, S. L. Bud'ko, J. L. McChesney, E. Rotenberg, T. Valla, A. V. Fedorov, P. C. Canfield, B. N. Harmon, and A. Kaminski, Phys. Rev. Lett. **101**, 177005 (2008).

[50] H. Suhl, J. Less Common Met. **62**, 225 (1978).

[51] T. K. Kopec and J. Klamut, Phys. Status Solidi B **137**, 73 (1986).

[52] C. R. Rotundu, W. Tian, K. C. Rule, T. R. Forrest, J. Zhao, J. L. Zarestky, and R. J. Birgeneau, Phys. Rev. B **85**, 144506 (2012).

[53] S. Avci, O. Chmaissem, E. A. Goremychkin, S. Rosenkranz, J.-P. Castellan, D. Y. Chung, I. S. Todorov, J. A. Schlueter, H. Claus, M. G. Kanatzidis, A. Daoud-Aladine, D. Khalyavin, and R. Osborn, Phys. Rev. B **83**, 172503 (2011).

[54] M. G. Kim, D. K. Pratt, G. E. Rustan, W. Tian, J. L. Zarestky, A. Thaler, S. L. Bud'ko, P. C. Canfield, R. J. McQueeney, A. Kreyssig, and A. I. Goldman, Phys. Rev. B **83**, 054514 (2011).

[55] A. Kreyssig, M. G. Kim, S. Nandi, D. K. Pratt, W. Tian, J. L. Zarestky, N. Ni, A. Thaler, S. L. Bud'ko, P. C. Canfield, R. J. McQueeney, and A. I. Goldman, Phys. Rev. B **81**, 134512 (2010).

[56] P. Wang, Z. M. Stadnik, J. Zukrowski, A. Thaler, S. L. Bud'ko, and P. C. Canfield, Phys. Rev. B **84**, 024509 (2011).

[57] H. Luo, R. Zhang, M. Laver, Z. Yamani, M. Wang, X. Lu, M. Wang, Y. Chen, S. Li, S. Chang, J. W. Lynn, and P. Dai, Phys. Rev. Lett. **108**, 247002 (2012).

[58] S. Nandi, M. G. Kim, A. Kreyssig, R. M. Fernandes, D. K. Pratt, A. Thaler, N. Ni, S. L. Bud'ko, P. C. Canfield, J. Schmalian, R. J. McQueeney, and A. I. Goldman, Phys. Rev. Lett. **104**, 057006 (2010).

[59] P. Marsik, K. W. Kim, A. Dubroka, M. Rössle, V. K. Malik, L. Schulz, C. N. Wang, C. Niedermayer, A. J. Drew, M. Willis, T. Wolf, and C. Bernhard, Phys. Rev. Lett. **105**, 057001 (2010).

[60] A. D. Christianson, M. D. Lumsden, S. E. Nagler, G. J. MacDougall, M. A. McGuire, A. S. Sefat, R. Jin, B. C. Sales, and D. Mandrus, Phys. Rev. Lett. **103**, 087002 (2009).

[61] D. K. Pratt, M. G. Kim, A. Kreyssig, Y. B. Lee, G. S. Tucker, A. Thaler, W. Tian, J. L. Zarestky, S. L. Bud'ko, P. C. Canfield, B. N. Harmon, A. I. Goldman, and R. J. McQueeney, Phys. Rev. Lett. **106**, 257001 (2011).

[62] T. Goltz, V. Zinth, D. Johrendt, H. Rosner, G. Pascua, H. Luetkens, P. Materne, and H.-H. Klauss, Phys. Rev. B **89**, 144511 (2014).

[63] T. Yildirim, Phys. C (Amsterdam) **469**, 425 (2009).

[64] Q. Huang, Y. Qiu, W. Bao, M. A. Green, J. W. Lynn, Y. C. Gasparovic, T. Wu, G. Wu, and X. H. Chen, Phys. Rev. Lett. **101**, 257003 (2008).

[65] S. E. Hahn, Y. Lee, N. Ni, P. C. Canfield, A. I. Goldman, R. J. McQueeney, B. N. Harmon, A. Alatas, B. M. Leu, E. E. Alp, D. Y. Chung, I. S. Todorov, and M. G. Kanatzidis, Phys. Rev. B **79**, 220511 (2009).

[66] R. Mittal, S. K. Mishra, S. L. Chaplot, S. V. Ovsyannikov, E. Greenberg, D. M. Trots, L. Dubrovinsky, Y. Su, T. Brueckel, S. Matsuishi, H. Hosono, and G. Garbarino, Phys. Rev. B **83**, 054503 (2011).

[67] L. Chauvière, Y. Gallais, M. Cazayous, A. Sacuto, M. A. Méasson, D. Colson, and A. Forget, Phys. Rev. B **80**, 094504 (2009).

[68] R. Housley, N. Erickson, and J. Dash, Nucl. Instrum. Methods **27**, 29 (1964)

[69] D. Barb, *Grundlagen und Anwendungen der Mössbauerspektroskopie* (Akademie-Verlag, Berlin, 1980).

[70] G. Lang, Nucl. Instrum. Methods **24**, 425 (1963).

[71] Z. Li, X. Ma, H. Pang, and F. Li, J. Phys.: Condens. Matter **23**, 255701 (2011).

[72] N. Ni, S. Nandi, A. Kreyssig, A. I. Goldman, E. D. Mun, S. L. Bud'ko, and P. C. Canfield, Phys. Rev. B **78**, 014523 (2008).

[73] F. Ronning, T. Klimczuk, E. D. Bauer, H. Volz, and J. D. Thompson, J. Phys.: Condens. Matter **20**, 322201 (2008).

[74] M. Abdel-Hafiez, L. Harnagea, S. Singh, U. Stockert, S. Wurmehl, N. Leps, R. Klingeler, A. U. B. Wolter, and B. Büchner, J. Phys.: Conf. Ser. **391**, 012120 (2012).

[75] N. Kumar, S. Chi, Y. Chen, K. G. Rana, A. K. Nigam, A. Thamizhavel, W. Ratcliff, S. K. Dhar, and J. W. Lynn, Phys. Rev. B **80**, 144524 (2009).

[76] J. K. Dong, L. Ding, H. Wang, X. F. Wang, T. Wu, G. Wu, X. H. Chen, and S. Y. Li, New J. Phys. **10**, 123031 (2008).

[77] R. S. Preston, Phys. Rev. Lett. **19**, 75 (1967).

[78] A. Blachowski, K. Ruebenbauer, J. Zukrowski, J. Przewonik, K. Wojciechowski, and Z. Stadnik, J. Alloys Compd. **494**, 1 (2010).

[79] A. Blachowski, K. Ruebenbauer, J. Zukrowski, K. Rogacki, Z. Bukowski, and J. Karpinski, Phys. Rev. B **83**, 134410 (2011).

[80] A. Carrington and F. Manzano, Phys. C (Amsterdam) **385**, 205 (2003).

[81] M. Abdel-Hafiez, P. J. Pereira, S. A. Kuzmichev, T. E. Kuzmicheva, V. M. Pudalov, L. Harnagea, A. A. Kordyuk, A. V. Silhanek, V. V. Moshchalkov, B. Shen, H.-H. Wen, A. N. Vasiliev, and X.-J. Chen, Phys. Rev. B **90**, 054524 (2014).

[82] C. Bernhard, A. J. Drew, L. Schulz, V. K. Malik, M. Rössle, C. Niedermayer, T. Wolf, G. D. Varma, G. Mu, H.-H. Wen, H. Liu, G. Wu, and X. H. Chen, New J. Phys. **11**, 055050 (2009).

[83] A. J. Drew, C. Niedermayer, P. J. Baker, F. L. Pratt, S. J. Blundell, T. Lancaster, R. H. Liu, G. Wu, X. H. Chen, I. Watanabe, V. K. Malik, A. Dubroka, M. Rossle, K. W. Kim, C. Baines, and C. Bernhard, Nat. Mater. **8**, 310 (2009).

[84] H. Luetkens, H.-H. Klauss, M. Kraken, F. J. Litterst, T. Dellmann, R. Klingeler, C. Hess, R. Khasanov, A. Amato, C. Baines, M. Kosmala, O. J. Schumann, M. Braden, J. Hamann-Borrero, N. Leps, A. Kondrat, G. Behr, J. Werner, and B. Buchner, Nat. Mater. **8**, 305 (2009).

[85] R. Khasanov, D. V. Evtushinsky, A. Amato, H.-H. Klauss, H. Luetkens, C. Niedermayer, B. Büchner, G. L. Sun, C. T. Lin, J. T. Park, D. S. Inosov, and V. Hinkov, Phys. Rev. Lett. **102**, 187005 (2009).

[86] N. Haberkorn, B. Maiorov, M. Jaime, I. Usov, M. Miura, G. F. Chen, W. Yu, and L. Civale, Phys. Rev. B **84**, 064533 (2011).

[87] Y.-B. Shi, Y.-B. Huang, X.-P. Wang, X. Shi, A. van Roekeghem, W.-L. Zhang, N. Xu, P. Richard, T. Qian, E. Rienks, S. Thirupathaiah, K. Zhao, C.-Q. Jin, M. Shie, and H. Ding, Chin. Phys. Lett. **31**, 067403 (2014).